# Diffusive Staircases in Shear: Dynamics and Heat Transport

Justin M. Brown<sup>a</sup> and Timour Radko<sup>a</sup>

<sup>a</sup> Naval Postgraduate School, Monterey, California

(Manuscript received 14 August 2020, in final form 17 March 2021)

ABSTRACT: Arctic staircases mediate the heat transport from the warm water of Atlantic origin to the cooler waters of the Arctic mixed layer. For this reason, staircases have received much due attention from the community, and their heat transport has been well characterized for systems in the absence of external forcing. However, the ocean is a dynamic environment with large-scale currents and internal waves being omnipresent, even in regions shielded by sea ice. Thus, we have attempted to address the effects of background shear on fully developed staircases using numerical simulations. The code, which is pseudospectral, solves the governing equations for a Boussinesq fluid with temperature and salinity in a shearing coordinate system. We find that—unlike many other double-diffusive systems—the sheared staircase requires three-dimensional simulations to properly capture the dynamics. Our simulations predict shear patterns that are consistent with observations and show that staircases in the presence of external shear should be expected to transport heat and salt at least twice as efficiently as in the corresponding nonsheared systems. These findings may lead to critical improvements in the representation of microscale mixing in global climate models.

KEYWORDS: Arctic; Convection; Diapycnal mixing; Heating; Shear structure/flows; Numerical analysis/modeling

## 1. Introduction

Double-diffusive staircases remain a subject of both academic interest and global climate significance. Staircases are regions characterized by well-mixed convective layers separated by sharp interfaces. The name "staircase" derives from the step-like appearance of temperature and salinity profiles through these layers. These staircases appear throughout the World Ocean (Foster and Carmack 1976; Neal et al. 1969; Boldrin and Rabbitti 1990), but the focus of this paper will be on the nature of the staircases in the Arctic thermocline. In the Arctic Ocean, warm and salty Atlantic water enters the Arctic basin and subducts beneath the colder and fresher waters of the upper Arctic. In much of the Arctic, there are also Pacific waters that sit below the mixed layer and above the Atlantic layer. At the top of the Atlantic Water layer is a thermocline, where the temperature and salinity increase with depth. In this region, staircases have been observed by Neal et al. (1969) and Neshyba et al. (1971) and more recently by Timmermans et al. (2008), Stranne et al. (2017), and Shibley et al. (2017). Of interest to climate studies, these staircases mediate the heat transport from the warm water of Atlantic origin to the Arctic halocline and therefore serve as an important process in determining the heat flux from the Atlantic water upward to the sea ice. Indeed, if all the heat from the Atlantic layer was transported into the mixed layer, it would be more than enough to melt the Arctic sea ice (Turner 2010). Thus, the heat and salinity fluxes of these staircases are of great interest to the scientific community. These have been characterized from a number of different studies, including a compilation by Kelley (1990) and more recently in a number of numerical experiments by Flanagan et al. (2013). Modeling the staircase fluxes properly is integral to understanding these systems, as shown

Corresponding author: Justin M. Brown, jmbrown2@nps.edu

by Bebieva and Timmermans (2019), who compared 1D models with different transport dynamics to observations in Arctic waters and demonstrated the paramount significance of staircase-induced mixing. Despite their importance in global models [see, e.g., the experiment by Turner and Veronis (2004)], the origin and behavior of these staircases are not well understood.

It is generally accepted that the formation and maintenance of thermohaline staircases requires double-diffusive processes (Stern 1969; Walin 1964). Double-diffusive convection (DDC) occurs in a fluid with multiple components (hereafter assumed to be temperature and salinity) with different molecular diffusivities and in which the system is stably stratified in density. The nondimensional parameter used to characterize double-diffusive convection is the density ratio:

$$R_{\rho}^{-1} = \frac{\beta^* \frac{\partial S^*}{\partial z^*}}{\alpha^* \frac{\partial T^*}{\partial z^*}},\tag{1}$$

where  $T^*$  is the temperature,  $S^*$  is the salinity,  $\alpha^*$  is the thermal expansion coefficient, and  $\beta^*$  is the haline contraction coefficient. As this paper will use both dimensional and nondimensional quantities, we use an asterisk to denote dimensional quantities. There are two primary forms of DDC: fingering convection, which occurs for a system that has warm and salty water overlying colder and fresher waters, and diffusive convection, which occurs for the opposite case [see Radko (2013) for more details]. The Arctic thermocline is of the latter configuration, so that will be the focus here. A linear stability analysis of an incompressible system reveals that water is unstable to diffusive convection if  $1 \le R_{\rho}^{-1} \le 1.14$ . Many experimental (Turner and Stommel 1964; Marmorino and Caldwell 1976) and numerical (Noguchi and Niino 2010) studies have shown that double-diffusive staircases arise naturally from the smaller-scale diffusive convection in this range. In the Arctic thermocline, the

density ratio is measured to be in the range  $2 \le R_{\rho}^{-1} \le 7$  (Shibley et al. 2017), well outside the range of linear instability. Thus, the origin of these staircases has remained a mystery.

Several plausible mechanisms for the production of these staircases have been proposed. In the presence of weak horizontal gradients, a region with a large density ratio can be susceptible to intrusions (Bebieva and Timmermans 2017). These interleaving structures do resemble double-diffusive staircases and may have the potential to slowly evolve into true staircases over time. Additionally, it has been shown in experiments that when such regions are heated from below, staircases may generate spontaneously (Turner 1968), and such behavior could arise naturally from the warm Atlantic water entering the Arctic basin. Another possible model for the Arctic thermocline is the thermohaline-shear instability, the theory of which was developed by Radko (2019). In this instability, the presence of vertical shear serves to extend the region of instability to higher density ratios. Radko (2016) and Brown and Radko (2019) showed that the addition of shear can lead to the development of staircases in systems that would not form staircases spontaneously in the absence of shear. The addition of shear to the model is appropriate as steady currents and internal waves both serve as ubiquitous sources of shear in the World Ocean. However, the effects of shear on the properties of an existing staircase remain woefully unexplored.

We thus turn to determining the effects of shear on such systems. A useful review of the effects of shear on diffusive convection is given by Kelley et al. (2003), and we will describe our system with similar terminology. We characterize the magnitude of shear with the Richardson number:

$$Ri = \frac{N^{*2}}{\left(\frac{\partial u^*}{\partial z^*}\right)^2},\tag{2}$$

where  $\partial u^*/\partial z^*$  is the vertical shear and  $N^*$  is the Brunt-Väisälä frequency, given by

$$N^{*2} = -\frac{g^*}{\rho_o^*} \frac{\partial \rho^*}{\partial z^*},\tag{3}$$

where  $\rho^*$  is the density perturbation away from the reference density  $\rho_0^*$  and  $g^*$  is the acceleration due to gravity. Typically, a fluid with Ri < 1/4 is susceptible to shear instabilities, but much higher Richardson numbers ( $\sim$ 10) were sufficient to trigger the thermohaline–shear instability (Radko 2016). Thus, it is imperative to characterize the effects of such shear on the properties of double-diffusive staircases. The effects of shear on DDC have been studied numerically (Yang et al. 2016; Zaussinger and Kupka 2018), analytically (Smyth and Kimura 2007; Konopliv et al. 2018), and experimentally (Linden 1974; Wells et al. 2001, though these experiments were for the saltfingering case). In particular, Zaussinger and Kupka (2018) were able to confirm the formation of layers in their bounded shear flow problem for strongly stratified flows of Arctic relevance (density ratios of 2–3).

This study uses numerical simulations to analyze the effect of shear on Arctic staircases and on the heat flux from diffusive convection. We find that models without shear underpredict thermal fluxes by a factor of 2 and haline fluxes by a factor of 3 for shear that is characteristic of the ocean. In addition, we also show that two-dimensional simulations of this phenomenon are inadequate to reproduce this result, showing instead a 25% decrease in the fluxes for the sheared case. This dissimilarity between two- and three-dimensional dynamics is in contrast to typical double-diffusive systems, which are often well represented by two-dimensional studies (see, e.g., Flanagan et al. 2013). The inability of two-dimensional models to fully capture the dynamics of the interaction between shear and convection has also been reported for one-component fluids. For instance, Lipps (1971) showed that vertical shear causes convection to transport momentum upgradient, which steepens shear and inhibits convection. This artifact, which is also realized in double-diffusive two-dimensional simulations, is inconsistent with observations of oceanographic staircases in the presence of static shear (see, e.g., Simpson et al. 1979; Padman 1994), which show that the convecting layers typically transport momentum downgradient.

This paper is organized as follows: section 2 contains the governing equations and formulation of the problem. Our nondimensionalization is also defined in section 2. The simulations are presented in section 3, which includes comparisons to observations, and we conclude with some discussion in section 4.

## 2. Governing equations and formulation

We perform numerical simulations with a Fourier-based pseudospectral code. This code is a modification of the model (PADDI) commonly used in earlier studies of thermohaline staircases (Traxler et al. 2011; Brown and Radko 2019). The present version is designed to represent effects of external shear. This model evolves temperature, salinity, and velocity for an incompressible fluid with a linear equation of state in a triply periodic domain. The quantities are evolved temporally using a combined third-order Adams-Bashforth scheme and backward differentiation formula. The pressure is calculated using the Patterson-Orszag method to ensure incompressibility (Orszag 1969). The code used in this work uses a 3/2 dealiasing scheme. For details on the implementation of all these methods and their use in spectral and psuedospectral codes, the authors recommend a review of Canuto et al. (2007).

These simulations integrate the Boussinesq governing equations in the absence of planetary rotation (see, e.g., Baines and Gill 1969):

$$\frac{\partial \mathbf{u}^*}{\partial t^*} + \mathbf{u}^* \cdot \nabla^* \mathbf{u}^* = -\frac{\nabla^* p^*}{\rho_0^*} + g^* (\alpha^* T^* - \beta^* S^*) \hat{\mathbf{z}}$$
$$+ \nu^* \nabla^{*2} \mathbf{u}^*, \tag{4}$$

$$\frac{\partial T^*}{\partial t^*} + \mathbf{u}^* \cdot \nabla^* T^* + w^* \frac{\partial \overline{T}^*}{\partial z^*} = \kappa_T^* \nabla^{*2} T^*, \tag{5}$$

$$\frac{\partial S^*}{\partial t^*} + \mathbf{u}^* \cdot \nabla^* S^* + w^* \frac{\partial \overline{S}^*}{\partial z^*} = \kappa_S^* \nabla^{*2} S^*, \tag{6}$$

$$\nabla^* \cdot \mathbf{u}^* = 0, \tag{7}$$

where  $\mathbf{u}^* \equiv (u^*, v^*, w^*)$  is the velocity,  $p^*$  is the pressure,  $T^*$  is the temperature perturbation away from a background temperature field given by  $\partial \overline{T}^*/\partial z^*z^* + T_0^*$ ,  $S^*$  is the salinity perturbation relative to the background salinity field given by  $\partial \overline{S}^*/\partial z^*z^* + S_0^*$ ,  $\nu^*$  is the dynamic viscosity, and  $\kappa_T^*$  and  $\kappa_S^*$  are the diffusivities of temperature and salinity, respectively. The background temperature and salinity gradients are assumed to be predetermined and constant. The choice of excluding the effects of planetary rotation is justified by the small scales of convective cells in the staircase—typically on the order of 2-4 m. Carpenter and Timmermans (2014) did investigate the effects of externally imposed rotation on diffusive staircases and found that—though they may be of importance for some deep staircases in the Arctic—the effect of rotation is weak for the staircases of the upper thermocline, which is the focus of this discussion. We will use  $\hat{\mathbf{x}}$ ,  $\hat{\mathbf{y}}$ , and  $\hat{\mathbf{z}}$  to denote the unit vectors in the x, y, and z directions, respectively. The density perturbation  $\rho^*$  away from the uniform reference value  $\rho_0^*$  is defined as

$$\rho^* = \rho_0^* \left[ -\alpha^* \left( T^* + \frac{\partial \overline{T}^*}{\partial z^*} z^* \right) + \beta^* \left( S^* + \frac{\partial \overline{S}^*}{\partial z^*} z^* \right) \right]. \tag{8}$$

This system can be nondimensionalized using the typical nondimensionalization for double-diffusive problems (see, e.g., Radko 2013). We let the unit of length [I] be defined as

$$[l] \equiv \left(\frac{\kappa_T^* \nu^*}{g^* \alpha^* \left| \frac{\partial \overline{T}^*}{\partial z^*} \right|} \right)^{1/4}.$$
 (9)

The reader may recognize that the associated thermal Rayleigh number for a convective layer is equal to its height in [I] to the fourth power. We define the time unit as  $[t] \equiv [I]^2/\kappa_T^*$ , the temperature unit as  $[T] \equiv [I]|\partial \overline{T}^*/\partial z^*|$ , the salinity unit as  $[S] \equiv (\alpha^*/\beta^*)[T]$ , the density unit as  $[\rho] \equiv \rho_0^* \alpha^*[T]$ , and the pressure unit as  $[\rho] \equiv \rho_0^* \kappa_T^* \nu^*/[I]^2$ . For any dimensional results, the values of these units are taken to be [I] = 0.01 m, [t] = 714 s,  $[T] = 1 \times 10^{-4}$ °C, and  $[S] = 6.25 \times 10^{-4}$  psu, which are typical for the ocean, and the thermal and haline perturbations are taken relative to  $T_0^* = 0$ °C and  $S_0^* = 35$  psu, respectively. Additionally, for the purpose of calculating the fluxes, the density is assumed to be  $\rho_0^* = 10^3 \text{kg m}^{-3}$ , and the specific heat capacity of water is assumed to be  $c_p^* = 4200 \, \text{J kg}^{-1} \, ^{\circ} \text{C}^{-1}$ . This results in the following nondimensional equations:

$$\frac{1}{\Pr}\left(\frac{\partial \mathbf{u}}{\partial t} + \mathbf{u} \cdot \nabla \mathbf{u}\right) = -\nabla p + (T - S)\hat{\mathbf{z}} + \nabla^2 \mathbf{u},\tag{10}$$

$$\frac{\partial T}{\partial t} + \mathbf{u} \cdot \nabla T - w = \nabla^2 T, \tag{11}$$

$$\frac{\partial S}{\partial t} + \mathbf{u} \cdot \nabla S - w R_0^{-1} = \tau \nabla^2 S, \tag{12}$$

$$\nabla \cdot \mathbf{u} = 0, \tag{13}$$

$$\rho = -(T - z) + (S - R_0^{-1} z), \tag{14}$$

where  $\Pr \equiv \nu^*/\kappa_T^*$  is the Prandtl number,  $\tau \equiv \kappa_S^*/\kappa_T^*$  is the inverse Lewis number, and  $R_0 \equiv [\alpha^*(\partial \overline{T}^*/\partial z^*)]/[\beta^*(\partial \overline{S}^*/\partial z^*)]$  is the density ratio of the background gradients. In this work, we consider only diffusive convection, where  $\partial \overline{T}^*/\partial z^* < 0$  and  $\partial \overline{S}^*/\partial z^* < 0$ .

To simulate the effects of external shear, a linear background shear flow is introduced, given by  $\bar{u}\hat{x}$ , where

$$\overline{u} = Az, \tag{15}$$

where A is the constant nondimensional shear rate. We can express A in terms of the background Richardson number, Ri:

$$Ri = \frac{-g*\alpha*\frac{\partial \overline{T}*}{\partial z*} + g*\beta*\frac{\partial \overline{S}*}{\partial z*}}{\left(\frac{\partial \overline{U}*}{\partial z*}\right)^{2}} = \frac{\Pr(R_{0}^{-1} - 1)}{A^{2}}.$$
 (16)

To introduce this background velocity, the system of governing equations is transformed into the sheared frame of reference, denoted with tildes:

$$\tilde{x} = x - Azt, \tag{17}$$

$$\tilde{y} = y, \tag{18}$$

$$\tilde{z} = z, \tag{19}$$

$$\tilde{t} = t. \tag{20}$$

We then decompose the velocity field into the background component and the perturbation in the sheared reference frame  $\tilde{u}$  as  $\mathbf{u} \equiv \tilde{\mathbf{u}} + Az\hat{\mathbf{x}}$ . Thus, the governing equations become

$$\frac{1}{\Pr} \left( \frac{\partial \tilde{\mathbf{u}}}{\partial \hat{t}} + \tilde{\mathbf{u}} \cdot \nabla \mathbf{u} \right) = -\nabla p + (T - S)\hat{\mathbf{z}} + \nabla^2 \tilde{\mathbf{u}}, \tag{21}$$

$$\frac{\partial T}{\partial \tilde{t}} + \tilde{\mathbf{u}} \cdot \nabla T - w = \nabla^2 T, \tag{22}$$

$$\frac{\partial S}{\partial \tilde{t}} + \tilde{\mathbf{u}} \cdot \nabla S - w R_0^{-1} = \tau \nabla^2 S, \tag{23}$$

$$\nabla \cdot \mathbf{u} = 0, \tag{24}$$

where the  $\nabla$  operator is still defined in terms of the original, nonsheared system:

$$\nabla = \left(\frac{\partial}{\partial x}, \frac{\partial}{\partial y}, \frac{\partial}{\partial z}\right) = \left(\frac{\partial}{\partial x}, \frac{\partial}{\partial \tilde{y}}, \frac{\partial}{\partial \tilde{z}} - A\tilde{t}\frac{\partial}{\partial \tilde{x}}\right). \tag{25}$$

Our spectral solutions to the governing equations then have the form

$$q = \sum_{l=-N_x}^{N_x} \sum_{m=-N_y}^{N_y} \sum_{n=-N_z}^{N_z} q_{l,m,n}(t) \exp(ilk_x \tilde{x} + imk_y \tilde{y} + ink_z \tilde{z}),$$
(26)

where  $N_x$ ,  $N_y$ , and  $N_z$  are the total number of Fourier modes in the  $\tilde{x}$ ,  $\tilde{y}$ , and  $\tilde{z}$  directions, and  $k_x$ ,  $k_y$ , and  $k_z$  are the lowest, nonzero wavenumbers in the domain, which is of size ( $\Gamma_x$ ,  $\Gamma_y$ ,  $\Gamma_z$ ). The use of this method was introduced by Rogallo (1981) for the purpose of investigating homogenous turbulence and is

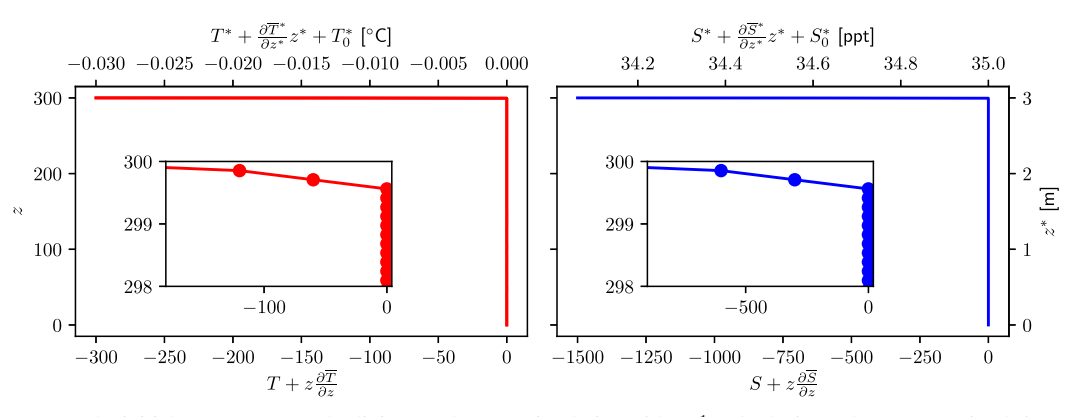


FIG. 1. The initial temperature and salinity profiles for a simulation with  $R_{\rho}^{-1} = 5$ . The inset shows a magnified view of the high-gradient region near the interface.

described in detail in Canuto et al. (2007). Note that the Fourier modes are periodic in the  $\tilde{z}$  direction, which is sheared with the mean flow. This proves to be problematic for integrating the system for an extended time as the grid will deform substantially. To address this problem, we introduce a remapping step as described in Canuto et al. (2007). When the simulation has evolved such that  $\Gamma_z A T$  is an integer multiple of  $\Gamma_x$  (i.e., the top-left point of the domain is directly over the bottom right), each (l, m, n) mode is shifted in phase by multiplying by  $\exp[-ilk_x At(z-z_{\rm mid})]$ , where  $z_{\rm mid}$  is the vertical midpoint of the domain, which serves to reorient the simulation to be vertical once again.

Each simulation is initialized by a single-layer staircase. Because the domain is vertically periodic, this effectively describes a staircase of infinite vertical extent with layers the size of the domain. The layer consists of a uniform temperature and salinity (seeded with small perturbations) with a highgradient interface. This interface is smoothed slightly to avoid numerical issues, as shown in Fig. 1. Each simulation is 300 units tall (and thus, the thermal Rayleigh number is  $8.1 \times$ 10<sup>9</sup>), which is equivalent to a dimensional height of 3 m. This is a reasonable choice for typical layer height in the upper thermocline of the Arctic, as shown in Shibley et al. (2017), who reported the results of an extensive survey of mean layer heights throughout the Arctic, finding them to typically be in the range of 0.5–3 m. The simulations are not sensitive to the exact structure of the initial conditions, as long as the step structure is sufficiently sharp.

We performed a total of eight three-dimensional simulations with density ratios of  $R_0 = [3,5,7]$  and with and without a shear characterized by Ri = 10. Six of these simulations were performed with  $\tau = 0.1$ , and two with  $\tau = 0.04$  for  $R_0 = 5$ , with and without shear, to accommodate computational limitations; our Prandtl number is chosen to be 10. This allows us to simulate parameters characteristic of the upper Arctic thermocline, which sees density ratios in the range 2–7 and has Richardson numbers of approximately 10 on average (Cole et al. 2014). The true value of  $\tau$  in the ocean is closer to 0.005; however, because the compositional diffusion length scale is the smallest physical scale in the system, it determines our minimum resolution. Other studies (see, e.g., Kimura and Smyth 2007;

Carpenter et al. 2012) have shown that lower values of  $\tau$  behave in a qualitatively similar way but tend to have higher fluxes than higher  $\tau$  simulations. Our simulations have a domain that spans  $300 \times 150 \times 300$  units in x, y, and z, respectively, resolved by  $768 \times 384 \times 1536$  grid points. The increased number of grid points in the vertical direction is designed to account for the grid deformation caused by the shearing coordinate system. There are some limitations of this setup in addition to the typical implications of incompressible studies of microstructure in the absence of planetary rotation. In particular, because the perturbations are periodic in the vertical direction, this constrains the height of the individual layers to be-at maximum-3 m, and this cannot change during the simulation as one might naturally expect the layers to evolve. Thus, there is no means for using this manner of simulation to address the typical scales of layers in the Arctic; however, the setup is reasonable for evaluating the flux through a staircase with a fixed step height.

### 3. Results

The simulation parameters are tabulated in Table 1 along with the time-averaged turbulent fluxes and the time-averaged thicknesses of the interface, which are defined in section 3a. Though the interface thicknesses are given in nondimensional units, they can also be interpreted as being in centimeters for oceanic values.

# a. Turbulent fluxes of heat and salt

We quantify the turbulent heat and salt transport by taking the product of the vertical velocity and the thermal and haline perturbations and average that quantity over space and time. These quantities are defined as follows:

$$F_T(t) \equiv \frac{1}{2\Delta t} \int_{t-\Delta t}^{t+\Delta t} \langle wT \rangle \, dt' \,, \tag{27}$$

$$F_{S}(t) = \frac{1}{2\Delta t} \int_{t-\Delta t}^{t+\Delta t} \langle wS \rangle \, dt', \qquad (28)$$

where the angled brackets indicate the average over the entire physical domain of the simulation and  $\Delta t$  defines the averaging

TABLE 1. The list of simulations and their associated turbulent fluxes and interfaces thicknesses.

$R_0^{-1}$	Ri	τ	$\overline{F}_T$	$\overline{F}_S$	$\overline{F}_T^* (\text{W m}^{-2})$	$\overline{F}_{S}^{*} \times 10^{-7} [\text{m (psu) s}^{-1}]$	$h_T$	$h_S$	$h_{ ho}$	$h_u$	$h_T/h_S$
3	∞	0.1	19.45	7.61	0.11	0.67	14.10	9.05	10.11	_	1.56
3	10	0.1	37.47	16.50	0.22	1.44	8.30	6.27	5.58	22.60	1.32
5	$\infty$	0.1	12.88	4.80	0.08	0.42	16.54	9.90	9.44	_	1.67
5	10	0.1	25.12	14.46	0.15	1.27	10.22	7.22	6.71	24.92	1.42
5	$\infty$	0.04	21.35	5.59	0.13	0.49	11.64	6.06	5.39	_	1.92
5	10	0.04	66.49	33.01	0.39	2.89	5.86	4.03	3.74	17.14	1.46
7	$\infty$	0.1	10.91	3.99	0.06	0.35	21.18	12.30	22.87	_	1.72
7	10	0.1	18.17	10.96	0.11	0.96	14.33	10.11	9.64	31.49	1.42

window, here set to be 10. The temporal average is used because the fluxes—in particular, the haline flux—vary strongly in time. The nondimensional turbulent fluxes are related to the Nusselt numbers  $Nu_T$  and  $Nu_S$  (the nondimensional ratio of total flux to diffusive flux) by

$$Nu_T - 1 = F_T, (29)$$

$$Nu_{s} - 1 = \frac{F_{s}}{\tau R_{0}^{-1}},$$
 (30)

and the nondimensional fluxes can be converted into their dimensional forms as the turbulent heat flux,  $F_T^* = \rho_0^* c_p^* F_T[l][T]/[t]$ ,

and haline flux,  $F_S^* = F_S[l][S]/[t]$ , respectively. In addition, we are also interested in characteristic fluxes through the convective layers. For this, we take an average from t=50 to t=250, which we will denote with an overbar as  $\overline{F_T}$  and  $\overline{F_S}$  for the thermal and haline fluxes, respectively. The choice of this time range is designed to allow for enough time to develop overturning convection and enough convective overturns to develop substantial statistics. We can estimate the overturning time by taking the ratio of the length traversed by a convective overturn (approximately twice the initial height of a convective cell, which is 300) and dividing by the characteristic velocity (approximately 100), which yields an overturning time of 6 time units. Thus, beginning our

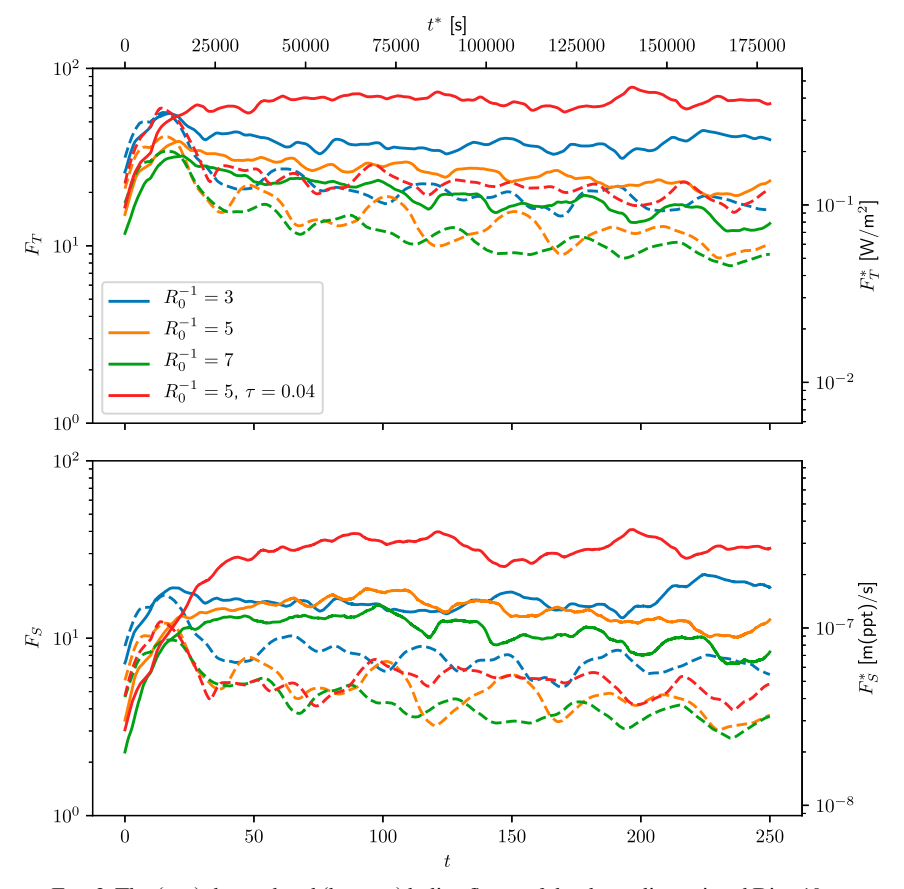


FIG. 2. The (top) thermal and (bottom) haline fluxes of the three-dimensional Ri=10 cases (solid lines) and the  $Ri=\infty$  cases (dashed lines). These fluxes are calculated using running averages using a window 20 time units wide.

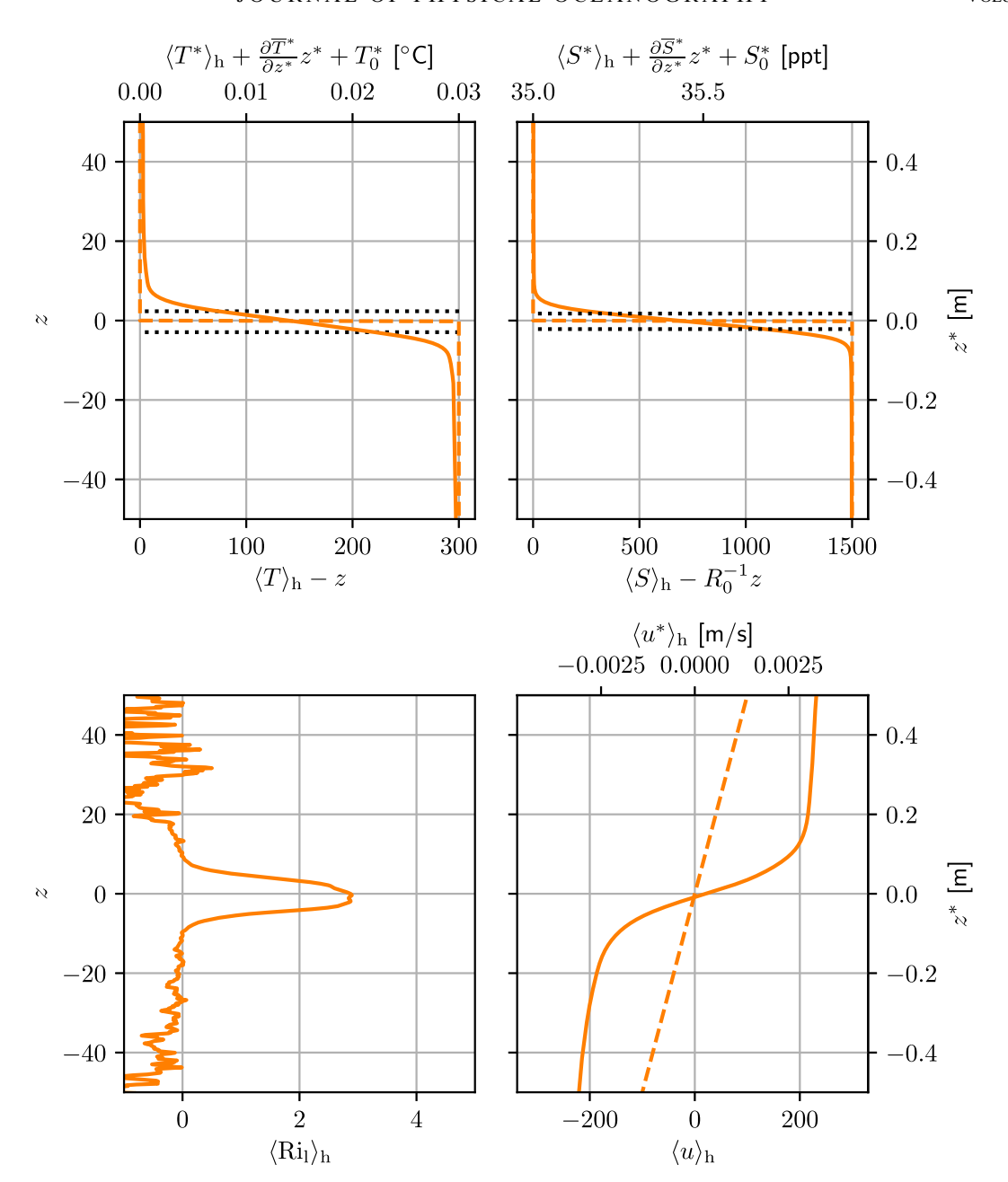


FIG. 3. A typical profile of the sheared simulation with  $R_0 = 5$  showing the (top left) temperature field, (top right) salinity field, (bottom left) local Richardson number, and (bottom right) u field. The profiles are taken at t = 68, after the convective onset has stabilized. The initial conditions are shown as dashed lines. Note that while the simulated domain extends from 0 to 300 in z, it is possible to use the periodicity of the perturbations to construct the field below the interface as well.

window at t = 50 ensures at least 8 convective overturns and ending at t = 250 provides at least 30 convective overturns to establish a reasonable statistical average.

The short-window flux averages are shown in Fig. 2 for both the sheared and the nonsheared cases. Early times (t < 20) are characterized by the development of overturning convection. The temperature diffuses across the interface more rapidly than the salinity, i.e., lowering the temperature at the top of the

layer and raising the temperature at the bottom (as seen, for example, in Fig. 3). This has the effect of raising the density at the top of the layer, resulting in the development of an unstable boundary at the interface, which then begins to overturn. As the simulations evolve, diffusive processes dominate at the interfaces, weakening the gradients of temperature and salinity; however, convection dominates in the layers, steepening the interfaces. These processes occur at different rates for

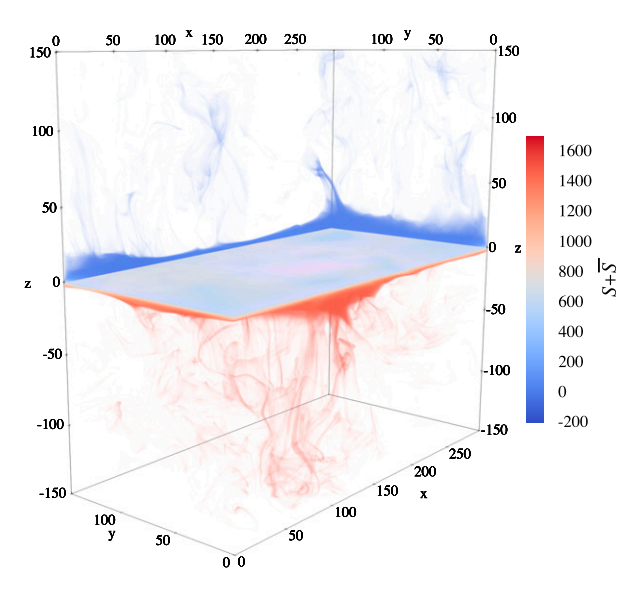


FIG. 4. A volume rendering of the salinity field at the interface for the simulation with  $\tau=0.04$ ,  $R_0^{-1}=5$ , and no externally imposed shear. The interface is located midway through the figure, and the opacity is chosen to highlight the interface.

temperature and salinity due to the differences in diffusivity and buoyancy of the two fields. During this time, the simulation fluxes grow substantially for both cases to comparable values for a given density ratio. This behavior is similar for both sheared and nonsheared flows. The simulations with lower density ratio (which are therefore closer to convective instability) show larger initial fluxes.

After the onset of convective instability, the behavior of the sheared and nonsheared systems show substantial differences from t = 20 to t = 50. The nonsheared simulations show a brief decrease in both thermal and haline fluxes by nearly a factor of 2 from the peak; however, the haline fluxes of the cases with Ri = 10 continue to grow until about t = 50, and the weakening of the thermal fluxes is lesser than in the nonsheared case. Conversely, the nonsheared simulations show decreasing fluxes from the peak near t = 20 to t = 50. This may be due to differences at the interface between the layers, the dynamics of which are quite different between the two cases, a fact that will be explored in more depth in section 3b. The interface must support the same net transport (diffusive plus turbulent) as the convective region. In the nonsheared case, the interfacial transport is largely diffusive in nature, but the additional application of shear could excite shear instabilities. The structure of the layer is shown in Fig. 3, which illustrates several horizontally averaged quantities, denoted with angled brackets and a subscript h. We define the interface thickness of a generic field q as

$$h_{q} \equiv \begin{vmatrix} \Gamma_{z} \frac{\partial \overline{q}}{\partial z} \\ \frac{\partial q}{\partial z} + \frac{\partial \overline{q}}{\partial z} \\ \frac{\partial \overline{q}}{\partial z} + \frac{\partial \overline{q}}{\partial z} \end{vmatrix}, \tag{31}$$

where  $\partial \overline{q}/\partial z$  represents the vertical derivative of the background field (e.g.,  $\partial \overline{T}/\partial z = -1$ ,  $\partial \overline{S}/\partial z = -R_0^{-1}$ ,  $\partial \overline{\rho}/\partial z = 1 - R_0^{-1}$ ,

and  $\partial \overline{u}/\partial z = A$ ). These locations are shown in Fig. 3 with black dotted lines. The time-averaged thickness for each simulation is provided in Table 1. The thermal boundary layer is thicker than the haline boundary layer in all cases. This is consistent with the observations by Sommer et al. (2013), which had comparable density ratios—even though the observed staircases were in Lake Kivu rather than the Arctic—and the simulations by Carpenter et al. (2012). We also investigate the ratio of these and find it is typically around 1.5, with the sheared simulations showing substantially sharper thermal interfaces by up to nearly a factor of 2. The ratio of  $h_T$  to  $h_S$  decreases in the sheared simulations by between 15% and 25%, although there does not appear to be a systematic trend with density ratio.

Close inspection of the properties of the interface reveal that it is subject to the Holmboe instability. This instability was theorized by Holmboe (1962) for a stably stratified fluid with a finite-width velocity interface. Such a system—even outside of the requisite conditions of the Kelvin–Helmholtz instability—can spontaneously develop and amplify traveling waves on this interface. The conditions for this amplification can be characterized in terms of the ratio between the thicknesses of the velocity interface and the density interface,  $h_u/h_\rho$ , and the Richardson number at the interface. We define a local Richardson number as

$$\operatorname{Ri}_{1} = -\frac{\frac{g^{*}}{\rho_{0}^{*}} \frac{\partial \rho^{*}}{\partial z^{*}}}{\left(\frac{\partial u^{*}}{\partial z^{*}}\right)^{2}} = \frac{\operatorname{Pr}\left(\frac{\partial T}{\partial z} - 1 - \frac{\partial S}{\partial z} + R_{0}^{-1}\right)}{\left(\frac{\partial u}{\partial z}\right)^{2}}, \quad (32)$$

and plot the horizontal average of this quantity in Fig. 3 to construct a Richardson number profile, finding a typical value of 3 at the interface. This is associated with an averaged shear of 5.84 for  $R_0^{-1} = 5$ , Ri = 10, which becomes roughly 0.008 s<sup>-1</sup> in dimensional units. Polyakov et al. (2019) measured the shear values in the interfaces for staircases in the Arctic ocean, finding shear on the order of 0.01 s<sup>-1</sup>, which is remarkably consistent with our results even though their work focused on intrusive processes, which may have different dynamics than the sheared staircase considered here. Under such circumstances, the Holmboe instability can only be dominant for  $h_u/h_\rho > 2$  (see, e.g., Alexakis 2005; Smyth and Carpenter 2019). For all the shearing simulations in this study, as listed in Table 1, this ratio is typically 4, well within a reasonable range to excite this instability and substantially altering the nature of the double-diffusive interface from the case without shear.

After t=50, all simulations achieve a steady behavior (see Fig. 2), which we use to characterize the fluxes of these systems. Taking the ratio of  $\overline{F_T}(\mathrm{Ri}=10)$  to  $\overline{F_T}(\mathrm{Ri}=\infty)$  and of the analogous haline fluxes, we find in general that both fluxes are substantially increased in the sheared case. The thermal flux for the sheared cases with  $\tau=0.1$ , is typically a factor of 2 higher than the case without shear, ranging from 1.93 for  $R_0^{-1}=3$ , 1.95 for  $R_0^{-1}=5$ , to 1.66 for  $R_0^{-1}=7$ . The increase in haline fluxes is larger, ranging from 2.17 for  $R_0^{-1}=3$ , 3.01 for  $R_0^{-1}=5$ , to 2.75 for  $R_0^{-1}=7$ . The fluxes do appear to slowly decrease in time, which is due to the slow diffusive smoothing of the interface.

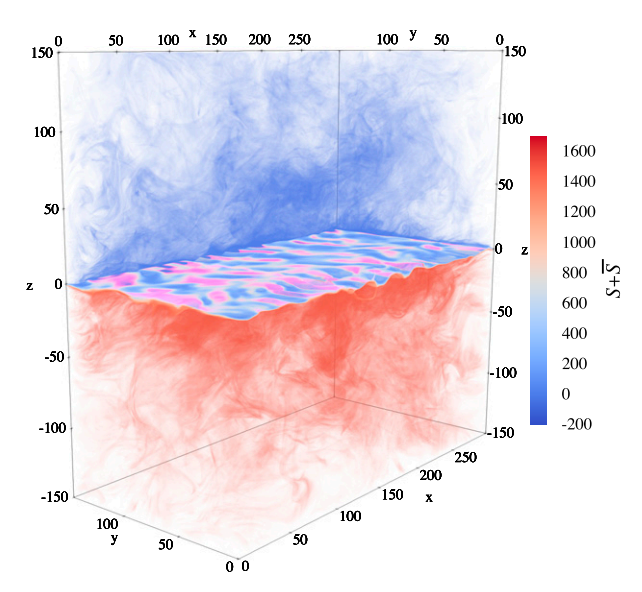


FIG. 5. A volume rendering of the salinity field at the interface for the simulation with  $\tau=0.04$ ,  $R_0^{-1}=5$ , and externally imposed shear. The color and opacity scales are identical to those of Fig. 4.

## b. Morphology

We show the morphology of the interface in Figs. 4 and 5, which reveal clear differences between the sheared and nonsheared cases. The sheared cases generally have anisotropic structures that are extended in the y direction (the cross-stream direction) but have short wavelengths in the x direction. A relevant comparison can be made to Blass et al. (2019), who simulated single-component convection in the presence of shear. They found-in their shear-dominated regime-the development of large-scale convective rolls with strong signatures at the interfaces, but those are quite distinct from the small-scale features found here, which are likely attributed to the Holmboe instability instead. The development of these small-scale structures substantially perturbs the interface, as is evident in Fig. 5. The interfaces in the nonsheared case show almost no motion; the interfaces in the sheared case appear to have small wave structures. Of greatest relevance, the motions across the interface permit greater transport through the interfaces themselves because the Holmboe waves distort the diffusive interface, which produces a larger surface area for diffusion. We attribute the limiting factor of the system to the interface because the mixing time scale of the interface (primarily diffusive) is much longer than that of the convective layer (primarily advective). However, it is true that shear serves to both strengthen the convection and promote more diffusive flux through the interface, and thus it is difficult to confidently attribute the increased fluxes primarily to any individual region of the system. The increase in convective transport in the sheared simulations is revealed (Fig. 5) by the more active small-scale turbulence. Though this behavior is generally consistent with the "shear-dominated regime" described by Blass et al. (2019), it is likely that the effects seen here are unique to the staircase

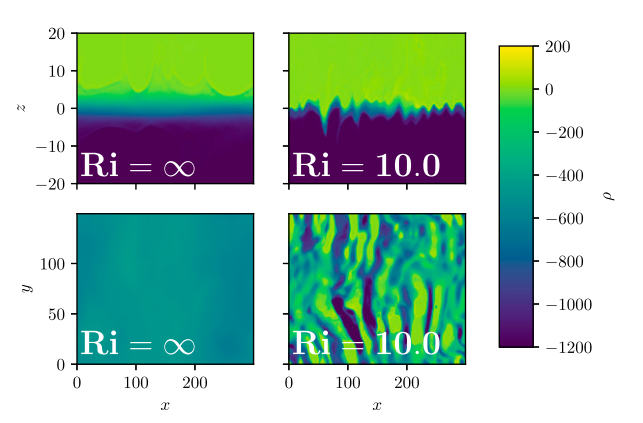


FIG. 6. Slices of the density field  $[S-T-(R_0^{-1}-1)z]$  of the simulations with  $\tau=0.04$ ,  $R_0^{-1}=5$  both (left) without and (right) with externally imposed shear. These slices are taken near the ends of the simulations, where  $t\approx250$ . (top) The side view, where we have only focused on the 40 length units around the interface, and (bottom) the top view at z=0.

setup as the boundaries of their work would not be subject to the Holmboe instability.

We also show the  $\rho$  field in Fig. 6. In this figure, the structure of the interface is more clearly shown in both the sheared and nonsheared cases. The former case highlights a much more defined interface, where the crests of the Holmboe instability appear starkly against the typical interface structure. The latter case shows a diffusive interface with only small density perturbations above and below. It is perhaps surprising that the more turbulent interface is sharper in density, but this is a common feature in double-diffusive systems, where turbulence tends to mix density upgradient and sharpens density interfaces. The interface perturbations appear to favor extended structures in the y direction with shorter extents in the x direction, giving the instability a quasi-two-dimensional structure; however, it is not possible to approximate this system in two dimensions, as is discussed in the appendix.

Figure 7 shows the inherent properties of the interface itself. In this, we include the total flux of buoyancy averaged over the interface, which we define as the region where the vertical gradient of density is greater than half its maximum, a region a few dimensionless length units thick. We designate the spatial average over this region with angled brackets and a subscript *i*. The buoyancy flux is given by the following (in dimensional and nondimensional forms):

$$F_{b}^{*} = g^{*}\beta^{*}\rho_{0}^{*} \left[ w^{*}S^{*} - \kappa_{S}^{*} \left( \frac{\partial S^{*}}{\partial z^{*}} + \frac{\partial \overline{S}^{*}}{\partial z^{*}} \right) \right]$$
$$- g^{*}\alpha^{*}\rho_{0}^{*} \left[ wT - \kappa_{T}^{*} \left( \frac{\partial T^{*}}{\partial z^{*}} + \frac{\partial \overline{T}^{*}}{\partial z^{*}} \right) \right], \tag{33}$$

$$F_b = \Pr\left(wS - \tau \frac{\partial S}{\partial z} + \tau R_0^{-1} - wT + \frac{\partial T}{\partial z} - 1\right). \tag{34}$$

The total fluxes include both the turbulent fluxes and the diffusive fluxes. Note that while the average of  $\partial T/\partial z$  over the entire domain is zero by construction, such is not the case

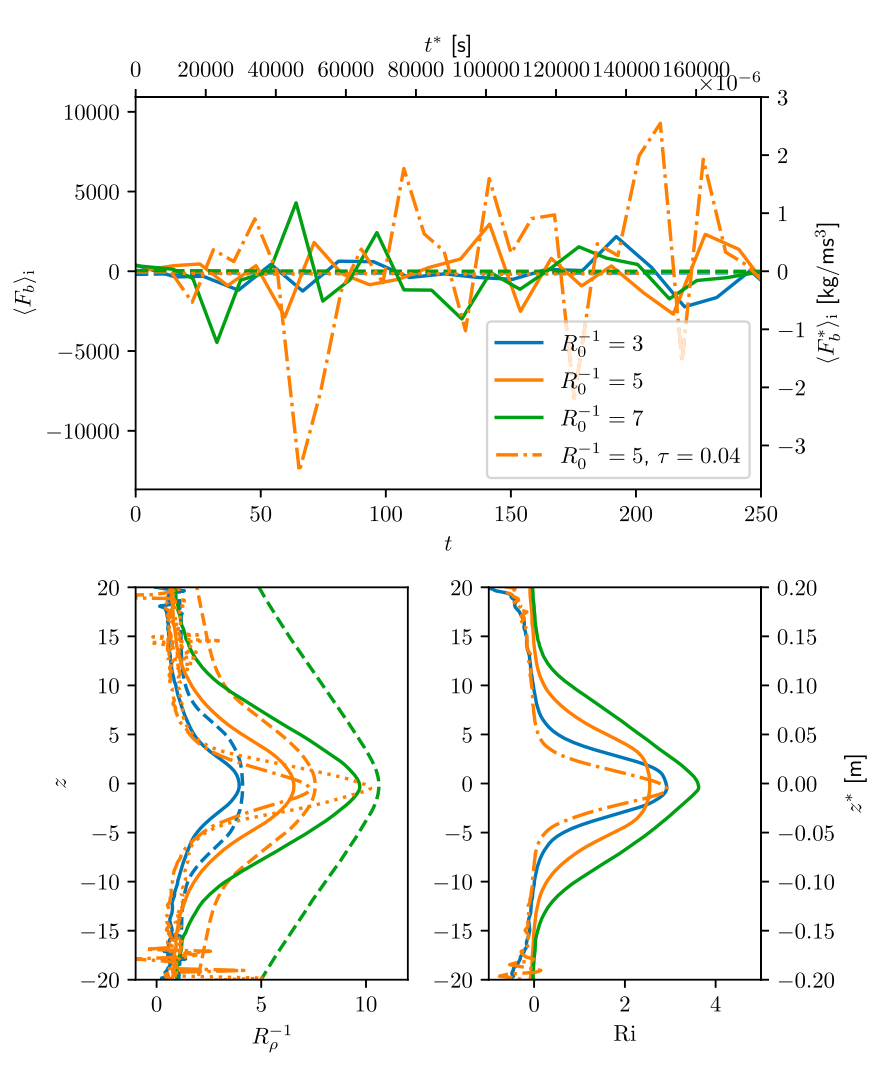


FIG. 7. (top) The total flux of temperature averaged over the interface for each simulation. The sheared simulations are plotted with solid lines, and the nonsheared simulations with dashed lines. Note that the fluxes of all the nonsheared simulations are very small by comparison and so are difficult to distinguish on this plot because they overlap near zero. (bottom left) The horizontally averaged density ratio profile for each simulation, using the same color and dashed scheme as in the flux figure. Note that the figure is zoomed in on the 40 length units around the interface. (bottom right) The horizontally averaged Richardson number profile for the sheared cases plotted in the same manner as the density ratio.

locally. Both the sheared and nonsheared simulations are plotted, but the sheared interface shows total fluxes that are much larger than the case without shear. This is due to the nature of the way the Holmboe waves (as described in section 3a) transport material through vertical oscillations, which is inherently a reversible mixing process that leads to very little net transport across the interface even though the instantaneous transport appears to be much larger than the stable interface from the case without shear.

We also show horizontally averaged profiles for the density ratio and the Richardson number in order to characterize the properties of the interfaces across the simulations. Here, we use the local definition of the density ratio  $R_{\rho}^{-1}$ . The density

ratio at the interface tends to be approximately the same as the global background density ratio. However, the sheared simulations do show higher density ratios, which is needed for the sharper density interfaces to exist. There do not appear to be many systematic changes in the Richardson number at the interface, which is typically in the range of 2–3, regardless of the global stratification of the system. This number is substantially less than the global value of the Richardson number, which is 10 for all the sheared cases. The interfaces do appear thicker in the cases with larger density ratios, and this behavior is also apparent in the trend of  $h_T$  in Table 1. This is consistent with the expected behavior of more stable stratification leading to weaker convection and therefore thicker interfaces.

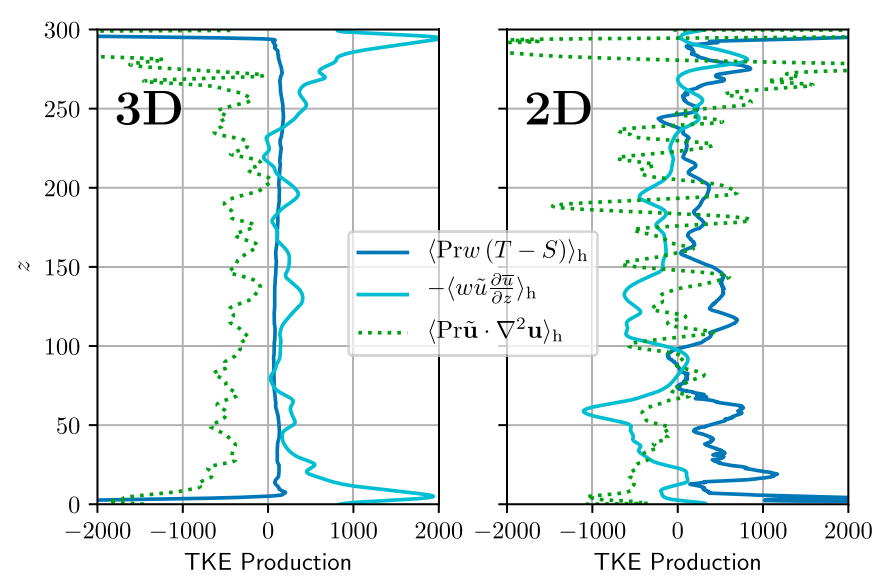


FIG. 8. Turbulent kinetic energy production at time  $t \approx 100$  for cases with  $R_0^{-1} = 5$  and Ri = 10 in (left) three dimensions and (right) two dimensions. The contributions due to buoyancy (blue), local shear (cyan), and viscous dissipation (dotted green) are averaged horizontally shown as a function of the vertical coordinate.

## c. Energetics

To address the physical reasoning for the increase in staircase fluxes with shear, we turn to arguments of energetics. The contributions of various physical processes to the production and dissipation of kinetic energy can be determined by taking  $\tilde{\mathbf{u}} \cdot (\partial/\partial t)\tilde{\mathbf{u}}$  from Eq. (10):

$$\frac{1}{2}\frac{\partial}{\partial t}\tilde{\mathbf{u}}^{2} + \frac{1}{2}\tilde{\mathbf{u}} \cdot \nabla \tilde{\mathbf{u}}^{2} = -\tilde{w}\tilde{u}\frac{\partial \overline{u}}{\partial z} + \Pr[-\nabla \cdot \tilde{\mathbf{u}}p + w(T - S) + \tilde{\mathbf{u}} \cdot \nabla^{2}\mathbf{u}], \tag{35}$$

where we have generalized  $\overline{u}$  to be a quasi-steady function of z that is evaluated by taking the horizontal average of our simulation. This choice permits us to identify sources of kinetic energy caused by local shear, which is largely concentrated near the interfaces. The sources and sinks of the turbulent kinetic energy are given as follows:  $-w\tilde{u}\partial\overline{u}/\partial z$  is the effect on kinetic energy by the local shear,  $-\Pr\nabla\cdot\tilde{\mathbf{u}}p$  is the reduction of kinetic energy by work done by the fluid,  $\Pr w(T-S)$  is the production of kinetic energy by buoyancy, and  $\Pr \tilde{\mathbf{u}}\cdot\nabla^2\mathbf{u}$  is the dissipation due to viscous effects.

To evaluate the energetics of the system, we take the horizontal averages of these terms and present them in Fig. 8. We also include a comparison in this figure to two-dimensional simulations, which are described in more detail in the appendix. However, it is evident from both the energetics and the general behavior of the two-dimensional simulations that these two setups are qualitatively different and that two-dimensional work is insufficient to simulate this phenomenon. In the three-dimensional case, it can be seen that shear promotes the production of turbulent kinetic energy everywhere, but in the two-dimensional case, the shear serves to counteract the production caused by buoyancy. In energy

balance in the three-dimensional case, this kinetic energy is lost to dissipation, as is expected. In the two-dimensional case, however, the buoyancy produces kinetic energy, which is reduced in roughly equal measure by the shear. This effect shows that the shear is, in effect, using the kinetic energy produced by buoyancy in order to transport the velocity upgradient in the simulation. This result was found for general two-dimensional convection in the presence of shear by Lipps (1971) and is described in more detail in the appendix.

#### 4. Conclusions

Vertical shear affects the heat flux through the Arctic thermohaline staircases. The thermal and haline fluxes are shown to increase by approximately a factor of 2 between cases with and without shear for a Richardson number of 10. We attribute this effect to structural changes in the interfaces of this system, which show a strong concentration of shear, consistent with the observations by Polyakov et al. (2019). We have found that our simulations produce comparable shear values and patterns as in the ocean. These interfaces are stable to the traditional double-diffusive instability with density ratios of 3–10 and to many shear instabilities with Richardson numbers of 2–3. However, we do see the development of a Holmboe instability at the interface, which shows features that are extended in the cross-stream direction but are smaller scale in the streamwise direction.

Estimates of heat transport based on laboratory-derived flux laws suggest that double diffusive convection adds approximately 0.22 W m<sup>-2</sup> heat transport to the sea ice in the Canadian Basin (Timmermans et al. 2008), but this is based on estimates from Kelley (1990), which do not include the effects of shear. Nonsheared direct numerical simulations by Flanagan et al. (2013)

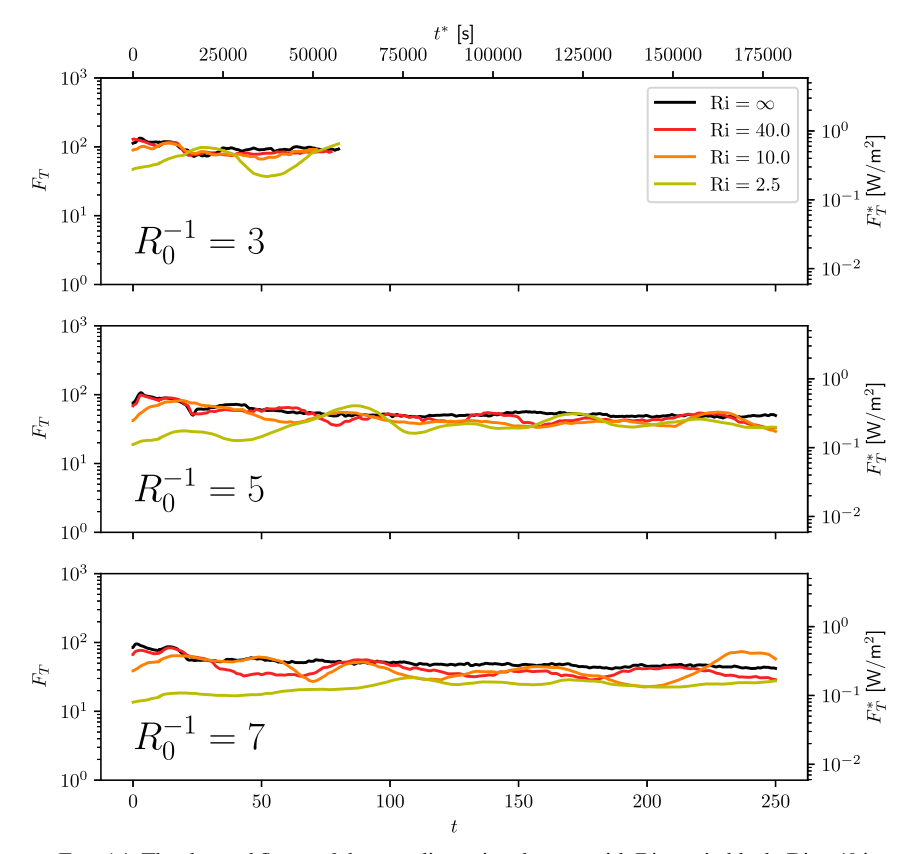


FIG. A1. The thermal fluxes of the two-dimensional cases, with  $Ri = \infty$  in black, Ri = 40 in red, Ri = 10 in orange, and Ri = 2.5 in yellow. These fluxes are calculated using running averages using a window 20 time units wide. (top) Simulations with a density ratio of 3, (middle) those with a density ratio of 5, and (bottom) those with a density ratio of 7.

suggest that these values may underestimate the heat flux by a factor of 2. The addition of shear's contribution to that heat flux, depending on the shear regime, may be significant enough to increase that value by an additional factor of 2. According to Kwok and Untersteiner (2011), the addition of approximately 1 W m<sup>-2</sup> can explain why the sea ice is melting at its current rate. The shear-induced intensification of double-diffusive transport revealed by our study can account for a substantial fraction of the required heat flux with the lowest  $\tau$  simulation with shear showing a heat flux of 0.4 W m<sup>-2</sup>. Extrapolating to oceanographic values of  $\tau$ , assuming a simple power law in terms of  $\tau$ , predicts fluxes in excess of 1 W m<sup>-2</sup>. Admittedly, this is a crude estimate based only on our  $R_0^{-1} = 5$  simulations and does not take into account the potential effects of intermittent shear, but it is suggestive that the effect of shear may be sufficient to compensate for all of the missing flux in this region. Since it is the goal of every environmental prediction system to present the most accurate forecast, the diapycnal mixing driven by a combination of shear and diffusive convection should be taken into account in operational and climate Arctic models. The results from this paper may assist in a more accurate prediction of when the Arctic may be sea ice free.

This research promotes several topics for future work. One additional consideration is the effect of  $\tau$ , which Kimura and

Smyth (2007) showed could have a quantitative impact on the final fluxes, with their  $\tau=0.04$  simulations having half the thermal flux of their  $\tau=0.01$  simulation. Thus, it is possible that decreasing  $\tau$  for our three-dimensional simulations to  $\tau=0.01$  could potentially increase these fluxes and may have an effect on the ratio of the flux with shear to that without. Another possible avenue of future work is the possibility of strong shear disrupting thermohaline staircases, which has empirical support from observations (Padman 1994; Guthrie et al. 2017). Such analysis would require investigating the three-dimensional simulations at a variety of Richardson numbers to determine the conditions of staircase collapse. The analysis of the effects of time-dependent shear, associated with internal waves, also represents an intriguing avenue of investigation.

Acknowledgments. The authors thank Jeff Carpenter and Igor Polyakov for their invaluable commentary on this publication. Support of the National Science Foundation (Grant OCE 1756491) is gratefully acknowledged. The first author received support through the National Research Council Research Associateship Program. The authors acknowledge the Texas Advanced Computing Center (TACC) at The University of Texas at Austin for providing HPC resources that

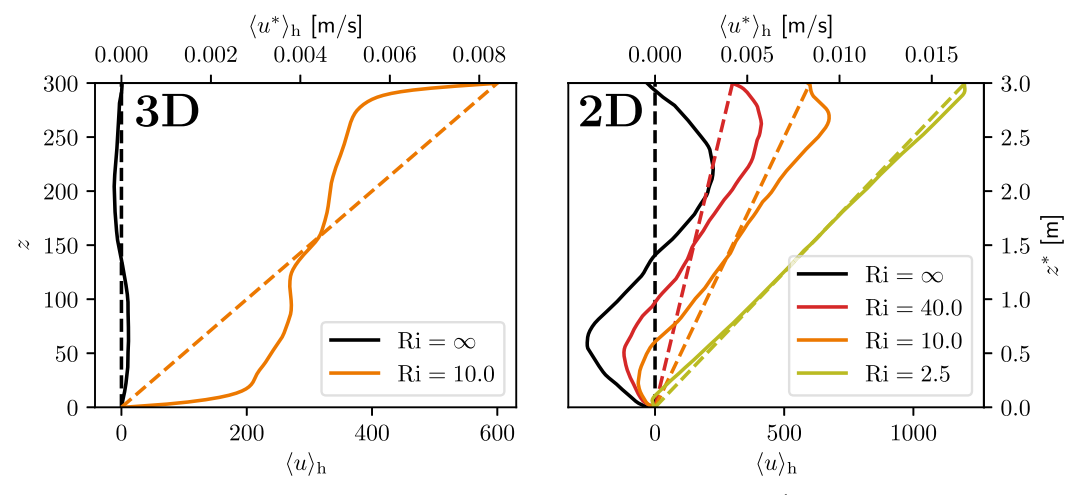


FIG. A2. The horizontally averaged velocity profile for all simulations with  $R_0^{-1} = 5$ : (left) three-dimensional simulations and (right) two-dimensional simulations. The color coding of the lines matches that of Fig. A1. The dashed lines show the initial linear shear profile.

have contributed to the research results reported within this paper (http://www.tacc.utexas.edu).

Datasets produced in this study are available in Mendeley Data: Brown, Justin (2020), "Diffusive Staircases in Shear: Data from Numerical Simulations," Mendeley Data, V2, doi: 10.17632/h87kvdzkv2.2.

## **APPENDIX**

## **Two-Dimensional Simulations**

We performed twelve two-dimensional simulations for all possible combinations of the density ratios of  $R_0 = [3, 5, 7]$  and Richardson numbers of Ri =  $[\infty, 40, 10, 2.5]$ , where a Richardson number of  $\infty$  represents a nonsheared case. This allows us to characterize a larger range of physical parameters and permits us to use a higher resolution in order to achieve  $\tau$  of 0.005, roughly consistent with the Arctic. Most of these simulations have 1024 Fourier modes on each side and resolve a domain that is 300 length units in the horizontal x direction and in the vertical z direction. The simulations with  $R_0 = 3$  proved to have more fine-scale features and so were resolved with 2048 Fourier modes on a side. In these cases, the factor limiting vertical resolution is the compositional diffusion scale rather than the grid deformation.

In Fig. A1, we investigate the trends of the long-window thermal and haline flux averages at equilibrium as a function of the density ratio and the Richardson number. The trend of fluxes as a function of density ratio has been well understood (see, e.g., Flanagan et al. 2013) with larger density ratios generally having lower fluxes. This phenomenon is due to larger density ratios (for a given thermal gradient) indicating a more strongly stratified system, which is thus less susceptible to convection. Unlike in the three-dimensional case, the addition of shear in the two-dimensional case can lower the fluxes by about 25%. As we will show, this effect is due to the interaction of convection and shear in different dimensionality, a subject

initially broached by Lipps (1971). And we can demonstrate this behavior most clearly by investigating the velocity structure in both systems.

Figure A2 shows the general structure of the velocity profile as a function of depth in all simulations with  $R_0^{-1} = 5$ . The main qualitative difference between two- and three-dimensional simulations is that the velocity within a layer is well mixed in the three-dimensional case, which reduces the shear inside the convective layer, but the opposite happens in two dimensions. The two-dimensional case tends instead to steepen shear within the convective layer, which tends to weaken and can reverse the shear at the interface. This is inconsistent with observations of shear in staircase interfaces, such as those of Polyakov et al. (2019). This turns out to be a general property of two-dimensional convection, which is shown most clearly in Lipps (1971), who displays how the addition of shear has a tendency to stabilize convection by upgradient transport of momentum within a convective region. It is thus suggestive that the regime of turbulence as measured in studies like those of Padman (1994) and Polyakov et al. (2019) is only achieved in three-dimensional studies, and while the response of twodimensional staircases to the effects of shear are academically interesting, it holds little practical value in oceanography.

### REFERENCES

Alexakis, A., 2005: On Holmboe's instability for smooth shear and density profiles. *Phys. Fluids*, 17, 084103, https://doi.org/ 10.1063/1.2001567.

Baines, P. G. G., and A. E. Gill, 1969: On thermohaline convection with linear gradients. *J. Fluid Mech.*, 37, 289–306, https:// doi.org/10.1017/S0022112069000553.

Bebieva, Y., and M.-L. Timmermans, 2017: The relationship between double-diffusive intrusions and staircases in the Arctic Ocean. *J. Phys. Oceanogr.*, 47, 867–878, https://doi.org/10.1175/JPO-D-16-0265.1.

—, and —, 2019: Double-diffusive layering in the Canada basin: An explanation of along-layer temperature and salinity

- gradients. *J. Geophys. Res. Oceans*, **124**, 723–735, https://doi.org/10.1029/2018JC014368.
- Blass, A., X. Zhu, R. Verzicco, D. Lohse, and R. J. A. M. Stevens, 2019: Flow organization and heat transfer in turbulent wall sheared thermal convection. *J. Fluid Mech.*, 897, A22, https:// doi.org/10.1017/JFM.2020.378.
- Boldrin, A., and S. Rabbitti, 1990: Hydrography of the brines in the Bannock and Tyro anoxic basins (eastern Mediterranean). *Mar. Chem.*, **31**, 21–33, https://doi.org/10.1016/0304-4203(90) 90029-C
- Brown, J. M., and T. Radko, 2019: Initiation of diffusive layering by time-dependent shear. *J. Fluid Mech.*, **858**, 588–608, https://doi.org/10.1017/jfm.2018.790.
- Canuto, C., M. Y. Hussaini, A. Quarteroni, and T. A. Zang, 2007: Spectral Methods: Evolution to Complex Geometries and Applications to Fluid Dynamics. Springer, 596 pp.
- Carpenter, J. R., and M.-L. Timmermans, 2014: Does rotation influence double-diffusive fluxes in polar oceans? *J. Phys. Oceanogr.*, 44, 289–296, https://doi.org/10.1175/JPO-D-13-098.1.
- —, T. Sommer, and A. Wüest, 2012: Simulations of a double-diffusive interface in the diffusive convection regime. *J. Fluid Mech.*, 711, 411–436, https://doi.org/10.1017/jfm.2012.399.
- Cole, S. T., M.-L. Timmermans, J. M. Toole, R. A. Krishfield, and F. T. Thwaites, 2014: Ekman veering, internal waves, and turbulence observed under Arctic Sea ice. *J. Phys. Oceanogr.*, 44, 1306–1328, https://doi.org/10.1175/JPO-D-12-0191.1.
- Flanagan, J. D., A. S. Lefler, and T. Radko, 2013: Heat transport through diffusive interfaces. *Geophys. Res. Lett.*, 40, 2466– 2470, https://doi.org/10.1002/grl.50440.
- Foster, T. D., and E. C. Carmack, 1976: Temperature and salinity structure in the Weddell Sea. *J. Phys. Oceanogr.*, **6**, 36–44, https://doi.org/10.1175/1520-0485(1976)006<0036: TASSIT>2.0.CO:2.
- Guthrie, J. D., I. Fer, and J. H. Morison, 2017: Thermohaline staircases in the Amundsen Basin: Possible disruption by shear and mixing. *J. Geophys. Res. Oceans*, **122**, 7767–7782, https://doi.org/10.1002/2017JC012993.
- Holmboe, J., 1962: On the behavior of symmetric waves in stratified shear layers. *Geofys. Publ.*, **24**, 67–113.
- Kelley, D. E., 1990: Fluxes through diffusive staircases: A new formulation. J. Geophys. Res., 95, 3365–3371, https://doi.org/ 10.1029/JC095iC03p03365.
- ——, H. J. S. Fernando, A. E. Gargett, J. Tanny, and E. Özsoy, 2003: The diffusive regime of double-diffusive convection. *Prog. Oceanogr.*, **56**, 461–481, https://doi.org/10.1016/S0079-6611(03)00026-0.
- Kimura, S., and W. Smyth, 2007: Direct numerical simulation of salt sheets and turbulence in a double-diffusive shear layer. *Geophys. Res. Lett.*, 34, L21610, https://doi.org/10.1029/ 2007GL031935.
- Konopliv, N., L. Lesshafft, and E. Meiburg, 2018: The influence of shear on double-diffusive and settling-driven instabilities. *J. Fluid Mech.*, **849**, 902–926, https://doi.org/10.1017/jfm.2018.432.
- Kwok, R., and N. Untersteiner, 2011: The thinning of Arctic Sea ice. Phys. Today, 64, 36–41, https://doi.org/10.1063/1.3580491.
- Linden, P. F., 1974: Salt fingers in a steady shear flow. *Geophys. Astrophys. Fluid Dyn.*, 6, 1–27, https://doi.org/10.1080/03091927409365785
- Lipps, F. B., 1971: Two-dimensional numerical experiments in thermal convection with vertical shear. J. Atmos. Sci., 28, 3–19, https:// doi.org/10.1175/1520-0469(1971)028<0003:TDNEIT>2.0.CO;2.

- Marmorino, G. O., and D. R. Caldwell, 1976: Heat and salt transport through a diffusive thermohaline interface. *Deep-Sea Res. Oceanogr. Abstr.*, **23**, 59–67, https://doi.org/10.1016/0011-7471(76)90808-1.
- Neal, V. T., S. Neshyba, and W. Denner, 1969: Thermal stratification in the Arctic Ocean. *Science*, 166, 373–374, https://doi.org/10.1126/science.166.3903.373.
- Neshyba, S., V. T. Neal, and W. Denner, 1971: Temperature and conductivity measurements under ice island T-3. *J. Geophys. Res.*, 76, 8107–8120, https://doi.org/10.1029/JC076i033p08107.
- Noguchi, T., and H. Niino, 2010: Multi-layered diffusive convection. Part I. Spontaneous layer formation. *J. Fluid Mech.*, 651, 443–464, https://doi.org/10.1017/S0022112009994150.
- Orszag, S. A., 1969: Numerical methods for the simulation of turbulence. *Phys. Fluids*, **12**, II–250, https://doi.org/10.1063/1.1692445.
- Padman, L., 1994: Momentum fluxes through sheared oceanic thermohaline steps. J. Geophys. Res., 99, 22 491–22 499, https:// doi.org/10.1029/94JC01741.
- Polyakov, I. V., L. Padman, Y. D. Lenn, A. Pnyushkov, R. Rember, and V. V. Ivanov, 2019: Eastern Arctic Ocean diapycnal heat fluxes through large double-diffusive steps. *J. Phys. Oceanogr.*, 49, 227–246, https://doi.org/10.1175/JPO-D-18-0080.1.
- Radko, T., 2013: Double-Diffusive Convection. Cambridge University Press, 342 pp.
- —, 2016: Thermohaline layering in dynamically and diffusively stable shear flows. *J. Fluid Mech.*, **805**, 147–170, https://doi.org/ 10.1017/jfm.2016.547.
- ——, 2019: Thermohaline-shear instability. Geophys. Res. Lett., 46, 822–832, https://doi.org/10.1029/2018GL081009.
- Rogallo, R. S., 1981: Numerical experiments in homogeneous turbulence. NASA Tech. Memo. 81315, 91 pp., https://ntrs.nasa.gov/api/citations/19810022965/downloads/19810022965. pdf.
- Shibley, N. C., M.-L. Timmermans, J. R. Carpenter, and J. M. Toole, 2017: Spatial variability of the Arctic Ocean's double-diffusive staircase. *J. Geophys. Res. Oceans*, 122, 980–994, https://doi.org/10.1002/2016JC012419.
- Simpson, J. H., M. R. Howe, N. C. G. Morris, and J. Stratford, 1979: Velocity shear in the steps below the Mediterranean outflow. *Deep Sea Res.*, **26A**, 1381–1386, https://doi.org/10.1016/0198-0149(79)90005-0.
- Smyth, W. D., and S. Kimura, 2007: Instability and diapycnal momentum transport in a double-diffusive, stratified shear layer. J. Phys. Oceanogr., 37, 1551–1565, https://doi.org/10.1175/JPO3070.1.
- —, and J. R. Carpenter, 2019: *Instability in Geophysical Flows*. Cambridge University Press, 328 pp.
- Sommer, T., J. Carpenter, M. Schmid, R. Lueck, M. Schurter, and A. Wuest, 2013: Interface structure and flux laws in a natural double-diffusive layering. *J. Geophys. Res. Oceans*, 118, 6092– 6106, https://doi.org/10.1002/2013JC009166.
- Stern, M. E., 1969: Collective instability of salt fingers. *J. Fluid Mech.*, **35**, 209–218, https://doi.org/10.1017/S0022112069001066.
- Stranne, C., and Coauthors, 2017: Acoustic mapping of thermohaline staircases in the Arctic Ocean. Sci. Rep., 7, 15192, https://doi.org/10.1038/s41598-017-15486-3.
- Timmermans, M.-L., J. Toole, R. Krishfield, and P. Winsor, 2008: Ice-Tethered Profiler observations of the double-diffusive staircase in the Canada Basin thermocline. *J. Geophys. Res.*, **113**, C00A02, https://doi.org/10.1029/2008JC004829.
- Traxler, A. L., S. Stellmach, P. Garaud, T. Radko, and N. H. Brummell, 2011: Dynamics of fingering convection. Part I

- Small-scale fluxes and large-scale instabilities. *J. Fluid Mech.*, **677**, 530–553, https://doi.org/10.1017/jfm.2011.98.
- Turner, J. S., 1968: The behaviour of a stable salinity gradient heated from below. *J. Fluid Mech.*, **33**, 183–200, https://doi.org/10.1017/S0022112068002442.
- ——, 2010: The melting of ice in the Arctic Ocean: The influence of double-diffusive transport of heat from below. *J. Phys. Oceanogr.*, 40, 249–256, https://doi.org/10.1175/2009JPO4279.1.
- —, and H. Stommel, 1964: A new case of convection in the presence of combined vertical salinity and temperature gradients. *Proc. Natl. Acad. Sci. USA.*, **52**, 49–53, https://doi.org/ 10.1073%2FPNAS.52.1.49.
- —, and G. Veronis, 2004: The influence of double-diffusive processes on the melting of ice in the Arctic Ocean: Laboratory analogue experiments and their interpretation. *J. Mar. Syst.*, 45, 21–37, https://doi.org/10.1016/j.jmarsys.2003.06.002.

- Walin, G., 1964: Note on the stability of water stratified by both salt and heat. *Tellus*, **16A**, 389–393, https://doi.org/10.1111/j.2153-3490.1964.tb00175.x.
- Wells, M. G., R. W. Griffiths, and J. S. Turner, 2001: Generation of density fine structure by salt fingers in a spatially periodic shear. *J. Geophys. Res.*, **106**, 7027–7036, https://doi.org/10.1029/2000JC000620.
- Yang, Y., R. Verzicco, and D. Lohse, 2016: Vertically bounded double diffusive convection in the finger regime: Comparing no-slip versus free-slip boundary conditions. *Phys. Rev. Lett.*, **117**, 184501, https://doi.org/10.1103/PhysRevLett. 117.184501.
- Zaussinger, F., and F. Kupka, 2018: Layer formation in double-diffusive convection over resting and moving heated plates. *Theor. Comput. Fluid Dyn.*, **33**, 383–409, https://doi.org/10.1007/s00162-019-00499-7.